AIAA SciTech
5-9 January 2015, Kissimmee, Florida
53rd AIAA Aerospace Sciences Meeting

Applicability of Hybrid RANS/LES Models in Predicting Separation Onset of the AVT-183 Diamond Wing

Daniel A. Reasor Jr.*
Air Force Test Center, 412th Test Wing, Edwards AFB, CA, U.S.A.

Donald J. Malloy†
Air Force Test Center, Arnold Engineering Development Complex, Arnold AFB, TN, U.S.A

and

Derick T. Daniel‡
Aerospace Testing Alliance, Arnold AFB, TN, U.S.A.

This effort contributes to the understanding of hybrid RANS/LES turbulence model behavior for prediction of separation onset via an investigation of the accuracy and predictions of the SARC-DDES variant. The focus is not to interrogate the underlying assumptions of the turbulence model or flow solver employed, but to report the accuracy of flowfield and surface quantity predictions given the choices for grid topology, spatial and temporal resolution, and numerical schemes used. Grid convergence is shown to be difficult to demonstrate for flows of this type. Steady state SARC and unsteady SARC-DDES simulation results demonstrate utility for pre-test predictions, but fail to resolve relevant physics in some instances.

Nomenclature

c	=	chord, m
C_f	=	skin-friction coefficient
C_p	=	pressure coefficient
C_D	=	drag coefficient
C_L	=	lift coefficient
C_M	=	pitching moment coefficient
Ma	=	Mach number
Re	=	Reynolds number
St	=	Strouhal number
U_∞	=	freestream velocity, m/s
α	=	angle of attack, deg.
β	=	angle of sideslip, deg.
Δs	=	grid spacing, mm
Δt	=	time step, s
γ	=	separation probability

I. Introduction

A difficult phenomenon to predict with modern Reynolds-averaged Navier−Stokes (RANS) and hybrid turbulence models based on a combination of RANS and large-eddy simulation (LES) methods is the incipient separation from a relatively blunt leading edge on a swept wing. Wings with relatively blunt leading edges have a larger radius of curvature (by definition) and generate less adverse pressure gradients as a result. When the curvature is modest, there lacks massive separation and the point or region of separation is difficult to capture accurately. Once separated, the flow consists of small structures and requires a refined grid. An obvious limitation of employing a hybrid RANS/LES turbulence model for this type of separation prediction is that the RANS zone of the simulation will ultimately control the separation point. Furthermore, any prediction insufficiencies or limitations will

* Engineer, Engineering Testing Techniques Flight, AIAA Senior Member
† Aerodynamics Lead, Analysis and Evaluation Branch, AIAA Associate Fellow
‡ Engineer, Computational Simulation, Modeling & Analysis, AIAA Member

also be present in the hybrid RANS/LES model results[1]. Unfortunately, computational resources have yet evolved to a point where wall-modelled LES, much less wall-resolved LES, methodologies are applicable for problems of this type. Nevertheless, tools that have shown to be useful for predicting unsteady aerodynamic coefficients and loads, separation regions, and acoustics with acceptable error when applied to current and future airframe designs and technology are available. The ability of current tools to predict this sensitive phenomenon of leading edge separation is assessed in this work.

This investigation was undertaken as part of the NATO RTO Task Group AVT-183, "Reliable Prediction of Separated Flow Onset and Progression for Air and Sea Vehicles," which was established for assessing the reliable prediction of separation onset for flows through experimental and computational means. In particular, this collaboration is between two entities of the Air Force Test Center enterprise, i.e., the 412th Test Wing and Arnold Engineering Development Complex. The presentation of results begins with a systematic grid refinement study to assess whether or not force and moment coefficients are resolved sufficiently using the RANS turbulence model. Mean and standard deviation of the force and moment coefficients from unsteady hybrid RANS/LES simulations are compared to wind-tunnel results along with time-averaged spanwise distributions of C_p. These unsteady responses are presented in the time and frequency domain for force and moment coefficients and for C_p responses at the locations specified by the complementary wind-tunnel experiments. The separation location is quantified using the classification system of Simpson[2] for unsteady flows. Transition is not modeled for any simulation, but results are compared against wind tunnel results with free transition and two types of surface roughness.

II. Methodology

A. Computational Domain and Test Conditions

The details of the AVT-183 diamond wing geometry, experimental conditions, and setup are discussed by Boelens et al.[3] Nevertheless, the domain extent, freestream conditions, and the length and area values used to set up the numerical experiment and post-process the computed results are included herein. The experimental results include measurements with free transition and with numerous types of boundary layer tripping mechanisms / surface roughness. When compared to computational results, the experiments are introduced and labeled according to surface roughness.

The origin of the simulation coordinate system is located at the leading edge of the wing/peniche intersection. The extent of the domain is $[x_{\min}, x_{\max}]\times[y_{\min}, y_{\max}]\times[z_{\min}, z_{\max}]$ = [-2.4, 7.2]×[-0.09, 6.0]×[-6.0, 6.0] m where x is the streamwise, y is the spanwise, and z is the direction normal to the upper and lower wing surfaces. All simulations employ no-slip boundary conditions on the wing, peniche, and wind tunnel wall and contain a systematic growth of prism layers to capture the viscous boundary layer that evolves on those surfaces. The inlet specifies the freestream Mach number and angle of attack, α, while the outflow boundary condition extrapolates from the interior solution. The fluid is modeled as a Newtonian fluid with Sutherland's viscosity model governed by the compressible RANS equations, the equation of state for a calorically perfect gas, and a one-equation turbulence model referenced in the next subsection.

The length and area values used to post-process results are a mean aerodynamic chord of $\bar{c} = 0.8$ m, wing area of A_{ref}=0.394385 m^2, moment reference location of $\boldsymbol{x}_M$ = (0.490759 m, 0 m, 0 m), and pitching moment length scale of L_M=1.2 m. The dimensionless parameters used as input into the numerical experiments were a fixed freestream Mach number of Ma=0.15, fixed Reynolds number based on mean aerodynamic chord $Re_{\bar{c}} = 2.7 \times 10^6$, and discrete angles of attack of $\alpha = 10°,\ 11°,\ 12°,\ 13°,\ 14°,$ and $15°$ with an angle of sideslip, β=0° for all cases.

B. Solver and Numerical Schemes Employed

The *Fully Unstructured Navier–Stokes* node-centered compressible flow solver, known as FUN3D,[4,5] is developed and maintained by NASA Langley Research Center and was used for all the simulations discussed in this work. A standard setup of numerical schemes was employed for the low-speed simulations; the specific schemes employed are as follows: Roe-type inviscid fluxes (without limiter), Galerkin equivalent viscous fluxes, and an optimized 2nd-order accurate implicit time integration scheme (see Biedron et al.[5] and fun3d.larc.nasa.gov for details). A dimensional time step of $\Delta t = 10^{-4}$ s was used for the unsteady simulations discussed with a maximum number of sub-iterations set to 40 reaching a temporal floor error[5] of 5×10^{-2}. However, most time steps were able to converge in 15-20 sub-iterations.

The one-equation Spalart–Allmaras turbulence model[6] continues to be a commonly employed model to investigate numerous airframes and wind-tunnel experiments in the public and private sectors. The variant of Shur et al.[7] (see Rumsey[8], turbmodels.larc.nasa.gov for details) employs a rotation or streamline curvature correction to the

production term in the eddy-viscosity-transport equation to reduce the amount of eddy viscosity generated in flow fields of this type; this variant is referred to as the SARC model. In this model, the eddy viscosity production is reduced in regions where the vorticity exceeds the strain rate, e.g., a vortex core, where the pure rotation is expected to suppress turbulent fluctuations[9]. The SARC turbulence model variant is implemented in conjunction with the delay-detached eddy simulation (DDES) technique of Spalart et al.[10] for unsteady simulations. This variant was developed to address the shortcomings of the original detached-eddy simulation formulation in thick boundary layers and shallow separation regions[11]. Therefore, the unsteady turbulence model used will be referred to as SARC-DDES.

Each simulation of the finest grid took approximately 80 hours to compute 1.0 physical second using 768 cores (2.5 GHz AMD Opteron™ series processors) of the Garnet supercomputer located at the US Army Engineer Research and Development Center (ERDC). Approximately 800,000 CPU-core hours were used to compute the results presented in this work.

C. Separation Determination Criterion

For unsteady flows where separation is prevalent, quantitative definitions have been proposed[2] using the fraction of time that the flow moves downstream instead of simply looking at vanishing shear stress[12]. Incipient detachment (ID) occurs with instantaneous backflow 1% of the time (γ_{pu}=0.99); intermittent transitory detachment (ITD) occurs with instantaneous backflow 20% of the time (γ_{pu}=0.80); transitory detachment (TD) occurs with instantaneous backflow 50% of the time (γ_{pu}=0.50); and detachment (D) occurs where the time-averaged wall shear stress is zero. This classification system was recently used[13] to discuss separation in a shockwave boundary layer interaction study in which the probability of flow reversal for different shock intensities was presented as a function of streamwise location. The same system is used in this work quantify the presence and character of the primary and inboard vortices that originate from the leading edge of the AVT-183 diamond wing utilizing the assumption that separation occurs when the spanwise component of skin friction coefficient becomes negative, i.e., $C_{f,y}(\mathbf{x},t)<0$. The direction of the shear stress vector is pointing inboard at locations of negative $C_{f,y}$. Slices of the C_f vector were recorded at 1 kHz at 10 discrete x/c_r locations (coincident with the C_p locations) and post-processed for interpretation.

III. Results

A. Steady-State Results and Grid Convergence Study

Three systematically refined grids were used to ensure the effect of poor spatial resolution was not a primary influence on results. The details of the three hybrid grids are presented in Tables 1 and 2 and Figs. 1 and 2 where the number of nodes ranges from 2.85×10^6 to 14.8×10^6. Each grid is constructed using anisotropic leading and trailing edges via the T-Rex features of Pointwise® version 17.2R1 and contains four-sided tetrahedral as well as five-sided prism and pyramid elements. The leading and trailing edge resolution was held constant for all grids at 0.01% c_{root}, the spanwise grid resolution along the leading and trailing edges and the streamwise resolution along c_{root} is doubled from coarse to medium grids and then doubled again from medium to fine grids (see Table 2 for details). The first wall normal spacing (4.2×10^{-6} m) and the growth factor (1.2) were identical for each grid consistent with best practices[14] for employing RANS turbulence models. Unfortunately, these systematic grid refinement studies based on RANS results cannot reflect errors due to a lack of grid isotropy that can be potential error source for hybrid RANS/LES simulations[1].

Table 1: Node and cell counts of the three grids used in the convergence study.

Grid	Nodes	r	Cells	Tetrahedral	Prism	Pyramid
Coarse	2.85M	1.000	6.91M	1.93M (28%)	4.92M (71%)	0.058M (<1%)
Medium	7.20M	1.362	19.5M	7.81M (40%)	11.5M (59%)	0.119M (<1%)
Fine	14.8M	1.270	42.4M	19.7M (46%)	22.5M (53%)	0.236M (<1%)

Table 2: Grid spacing (leading edge, Δs_{LE}, trailing edge, Δs_{TE}, wall normal, Δs_n) as well as growth factor (expansion ratio) for BL prisms, *GF*, span-wise spacing, Δs_{span}, and number of divisions of the wing at the root chord, N_{root}, for the three grids employed.

Grid	Δs_{LE}	Δs_{TE}	Δs_n	GF	Δs_{span}	N_{root}
Coarse	0.12 mm	0.12 mm	0.0042 mm	1.2	7.0 mm	160
Medium	0.12 mm	0.12 mm	0.0042 mm	1.2	3.5 mm	320
Fine	0.12 mm	0.12 mm	0.0042 mm	1.2	1.7 mm	640

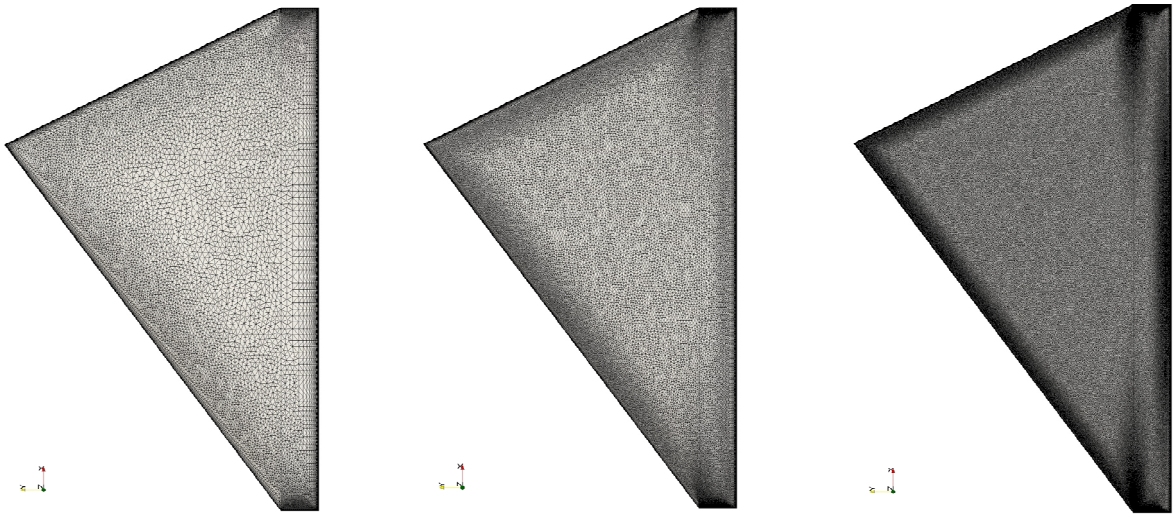

a) Coarse **b) Medium** **c) Fine**

Figure 1: Surface triangulations of the three grids employed.

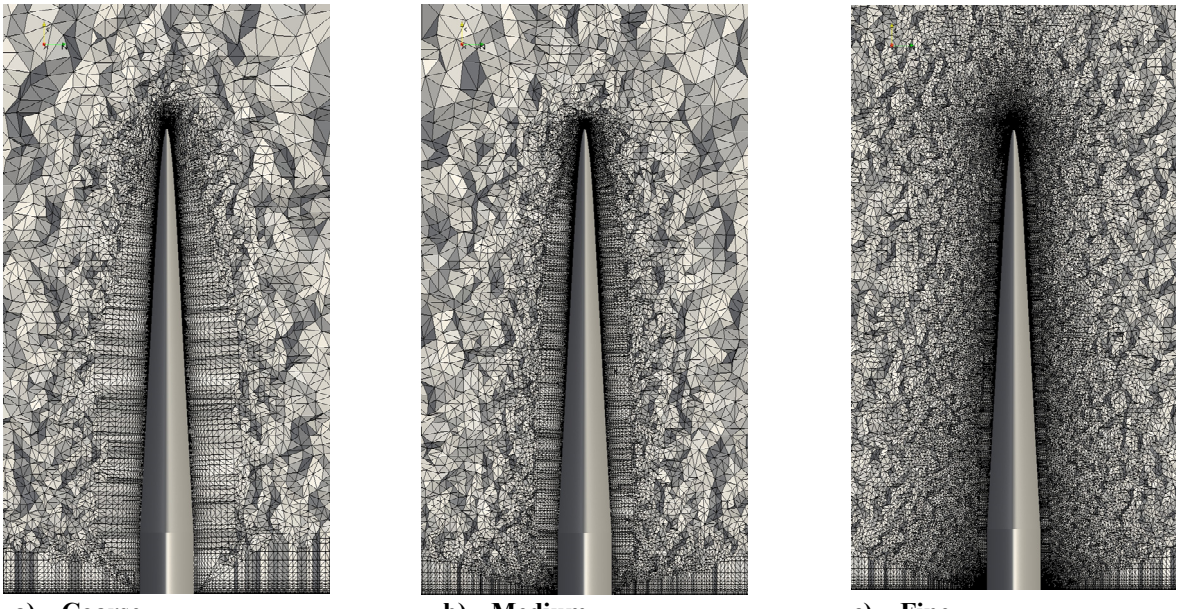

a) Coarse **b) Medium** **c) Fine**

Figure 2: Front view of the fluid domain discretization at x/c_r=0.6 of the three grids employed.

The grid refinement factor is defined[15] as

$$r = \left(\frac{N_1}{N_2}\right)^{1/d} \tag{1}$$

where N_1 and N_2 are the number of grid points in the finer and coarser of the two grids being compared respectively and d is the spatial dimension (three in our case) and is included in Table 1. The grid convergence index[16] (*GCI*) is defined as

$$GCI = \frac{F_s}{r^p - 1}\left|\frac{f_2 - f_1}{f_1}\right|, \tag{2}$$

where F_s is a safety factor of 3.0, p is the order of accuracy for the spatial scheme employed (2.0 is assumed here), and f_1, f_2 are the finer and coarser grid global solution quantities (C_L, C_D, C_M) considered.

The *GCI* values for the force and moment coefficients are provided in Table 3 for SARC simulations at α=12°. The *GCI* values are relatively low when comparing the coarse and medium grids, but increases significantly when comparing the medium and fine grids. These findings highlight grid sensitivities for SARC simulations where primary and inboard vortices have significant effects on the aerodynamic coefficients. The flow predicted using the fine grid, which contains more tetrahedral elements near the edge of the boundary layer than the medium and coarse grids and more spanwise resolution on the leading edge, separates earlier than the coarse and medium grids. This may indicate that the coarse and medium grids are not in the asymptotic range for comparison or that grid-induced separation may be present.

Table 3: Force and moment coefficients for the three grids used in the convergence study for at α=12°.

Grid	C_L	C_D	C_M	GCI_{C_L}	GCI_{C_D}	GCI_{C_M}
Coarse	0.5543	0.0843	-0.0231	-	-	-
Medium	0.5572	0.0841	-0.0226	1.769%	0.6577%	7.062%
Fine	0.5347	0.0840	-0.0209	20.41%	0.4772%	39.14%

The C_p distribution on the top surface for the three grids considered is presented in Fig. 3. Reference locations for x/c_r cut-planes are also included, but are not inclusive of all locations investigated in the TUM experiments discussed by Hövelmann et al.[17] Each of these simulations is run for 10^4 iterations and has reached a global residual of $O(10^{-10})$. The general region where the primary vortex originates is highlighted by C_p values (cooler colors in the contour plots). The origin of this vortex is very similar for the coarse and medium grids and is located immediately downstream of the x/c_r=0.295 location. However, for the fine grid, the origin is shifted upstream of the x/c_r=0.295 location resulting in a reduction of C_L. Also of note is the lack of smoothness in the contour for the medium grid in the vicinity of the x/c_r=0.500 location which is surprisingly not present in the fine grid result. While the location of the primary vortex does not affect the predicted C_D values by a large percentage, it does influence C_L significantly as seen in Table 3.

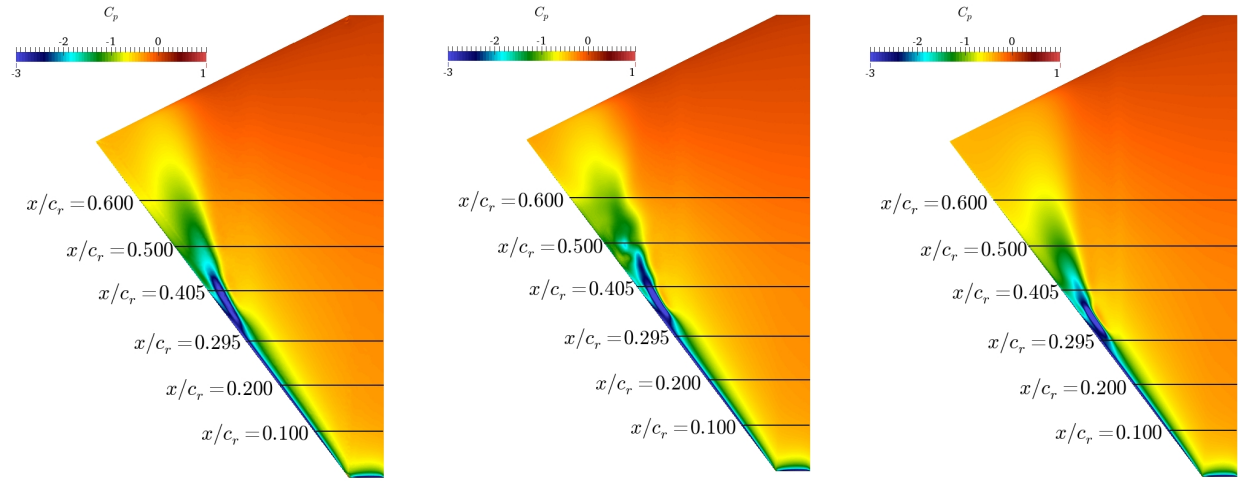

a) Coarse **b) Medium** **c) Fine**

Figure 3: Top view of the SARC C_p predictions at α=12° for the three grids employed.

The local influences of grid refinement are more evident when examining the C_p distribution at discrete chord locations. Figure 4 presents the C_p distribution at 6 chord locations for steady-state SARC simulations along with time-averaged experimental data[17] for the free transition and forced transition (110 μm trip grit and 150 μm trip dots) experiments at α=12°. Figure 4 illustrates that the free transition experiments separate further upstream than the forced transition experiments (as expected from the resiliency of turbulent boundary layers) evident by the inboard peak in C_p at the x/c_r=0.200 location. The SARC simulations assume that the flow is turbulent throughout the flowfield; therefore, any surface features influenced by transition will not be captured accurately. At the furthest upstream location of x/c_r=0.100, the wind tunnel and CFD results are nearly identical. As the vortex begins to form at the leading edge of the wing, the wind tunnel results begin to differentiate themselves and depart from the SARC predictions. It is known that SA-based models tend to under predict separation onset[1]. The 110 μm trip grit experimental results demonstrate the best correlation with the SARC predictions for the coarse and medium grids matching the pressure rise for x/c_r=0.405 very well, but over-predict the pressure rise at x/c_r=0.500. The fine grid reveals the onset of the leading edge vortex at x/c_r=0.295 whereas the coarse and medium grids predictions do not.

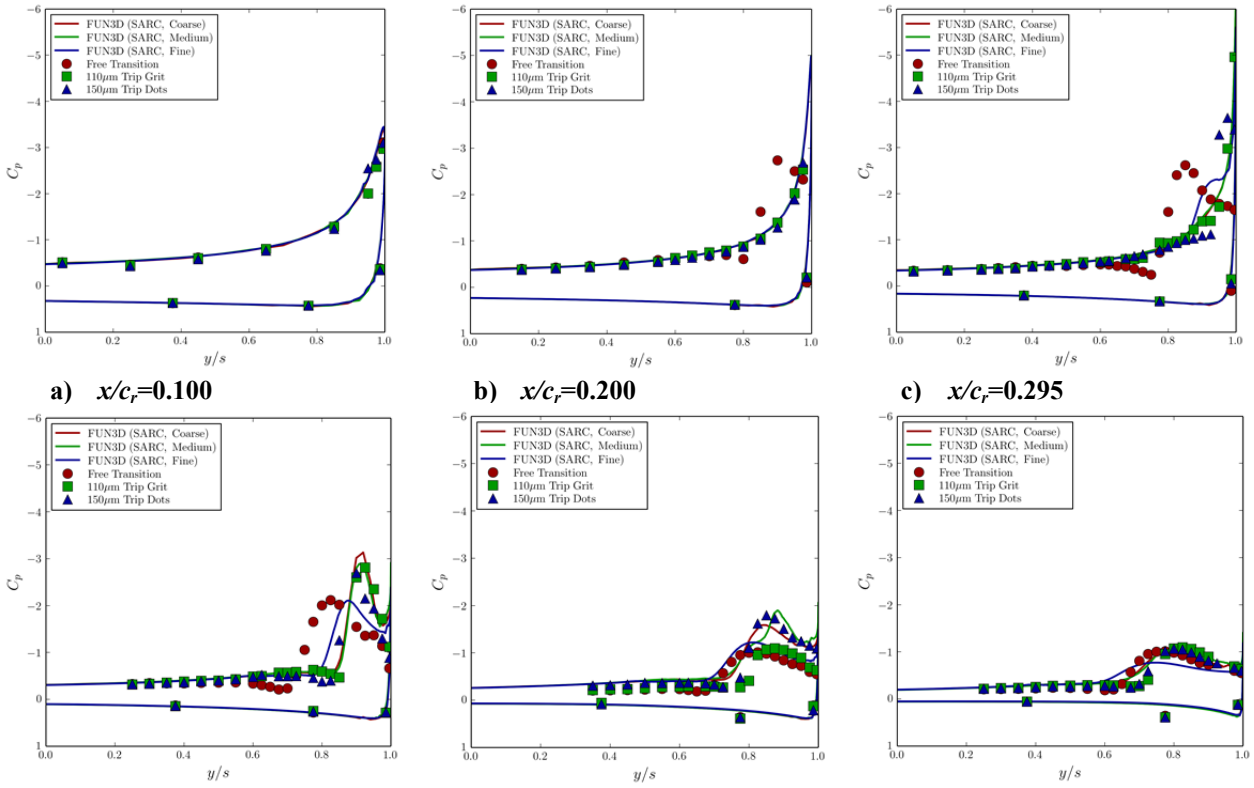

a) x/c_r**=0.100** **b)** x/c_r**=0.200** **c)** x/c_r**=0.295**

d) x/c_r**=0.405** **e)** x/c_r**=0.500** **f)** x/c_r**=0.600**

Figure 4: **Steady state (SARC) C_p comparisons for α=12° at six x/c_r locations for the three grids employed.**

The velocity field was measured experimentally at several chord locations (x/c_r = 0.1, 0.15, 0.2, 0.25, 0.295, 0.305, 0.35, 0.395, 0.405, 0.45, 0.5, 0.55, and 0.6) for the α=12° condition by TUM using particle-image velocimetry (PIV) as presented by Hövelmann et al.[18] The PIV results were taken from the flowfield over the wing with the 150 μm sized trip dots. Figure 5 compares the individual components of the velocity field (normalized by the freestream velocity, U_∞) measured via PIV with the predictions of the FUN3D steady-state SARC simulations for the three grids.

Figure 5(a-d) compares u/U_∞ of the experiment to the SARC predictions. The primary vortex is visible via a region of the u/U_∞ field that is lower than unity. The minimum velocities for each cut-plane are found in the center of the primary vortex which continues to reduce as the flow travels downstream to the PIV window position of x/c_r=0.600. The CFD results generally correlate with the PIV measurements. The u/U_∞ velocity field results for the coarse grid in Fig. 5(b) predict a vortex very similar in size to the PIV results, the medium grid prediction (provided in Fig. 5(c)) of the primary vortex topology has a less elliptical cross-section than the coarse prediction. Lastly, the fine grid prediction in Fig. 5(d) shows a noticeably larger vortex than that observed in the experiments. Differences

in the v/U_∞ and w/U_∞ velocity results are less noticeable in Fig. 5(e-l), but the non-uniform result for the medium grid is prevalent over the PIV measurements as well as the coarse and fine grid SARC predictions.

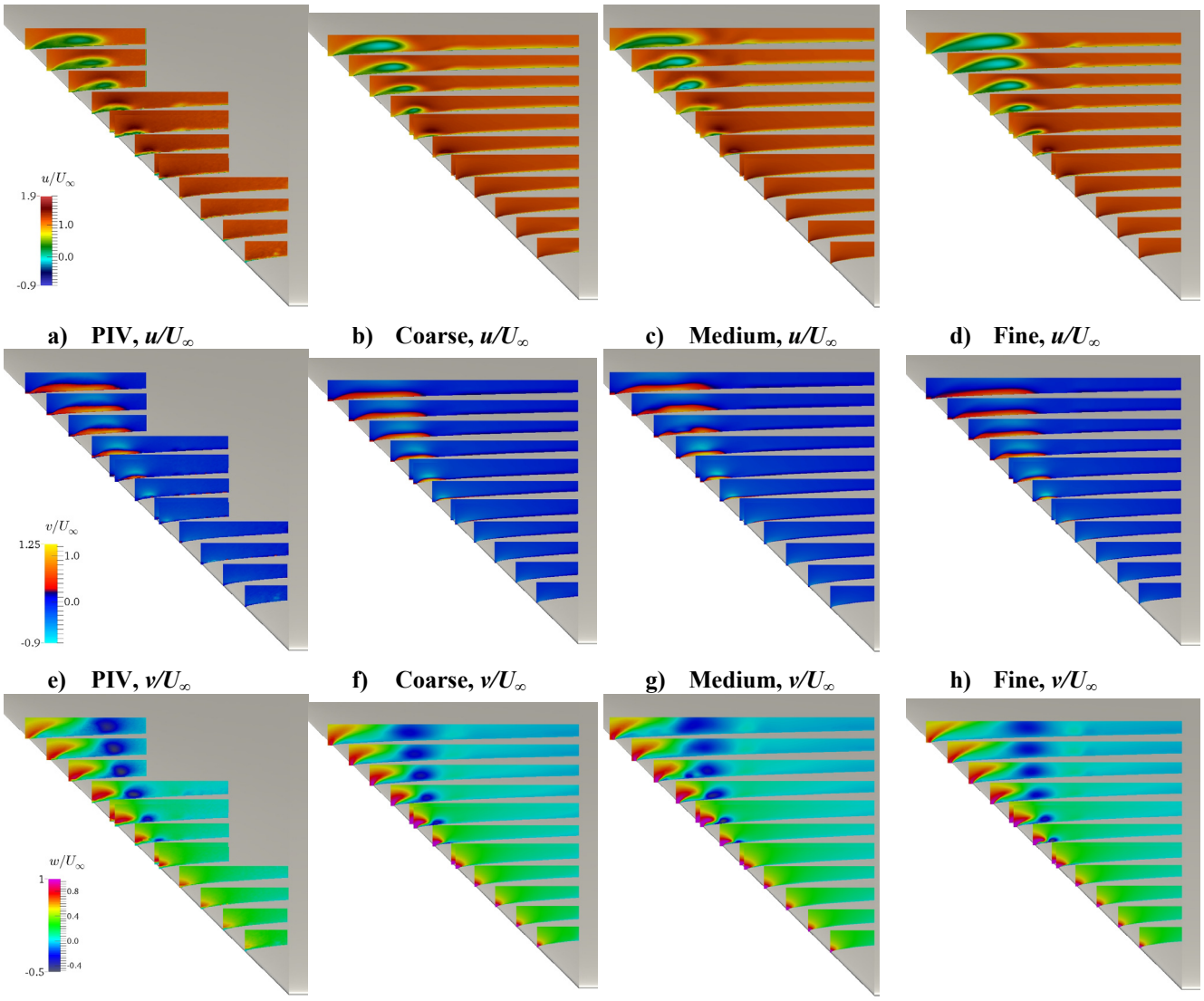

a) PIV, u/U_∞ b) Coarse, u/U_∞ c) Medium, u/U_∞ d) Fine, u/U_∞

e) PIV, v/U_∞ f) Coarse, v/U_∞ g) Medium, v/U_∞ h) Fine, v/U_∞

i) PIV, w/U_∞ j) Coarse, w/U_∞ k) Medium, w/U_∞ l) Fine, w/U_∞

Figure 5: Flowfield comparisons of TUM PIV measurements[18] and steady state (SARC) predictions of normalized velocity components at α=12° with results presented at the cut planes of the PIV windows.

B. Time-Averaged Results

The focus of this work is on the assessment of hybrid RANS/LES models for simulating unsteady vortex-dominated flows with leading edge separation. As a result, comparisons were performed with time-averaged quantities and frequency-domain responses. Time averaging was performed using the final 0.9 s (0.1-1.0 s) of the time histories to remove any initial transients from the statistics. Sampling of force and moment coefficients was done at 10 kHz (or every time step) while spanwise cuts for pressure and skin friction coefficient analysis was done at 1 kHz (or every 10 time steps).

The large primary vortex separating from the leading edge grows larger with increasing α. As the vortex becomes larger, the magnitude of the unsteadiness in force and moment coefficients is observed to increase as well. Table 4 presents the time-averaged mean and standard deviation of the force and moment coefficients for six discrete values of α using the SARC-DDES turbulence model with the fine grid introduced in the grid-convergence

study of the previous section. An increase in unsteadiness with increasing α is corroborated by the standard deviations, σ, of each of the coefficients in Table 4.

Table 4: Time-averaged mean, μ, and standard deviation, σ, of C_L, C_D, and C_M computed for the 0.1-1.0 s time interval.

	α=10°	α=11°	α=12°	α=13°	α=14°	α=15°
μ_{CL}	0.444	0.491	0.541	0.591	0.635	0.685
σ_{CL}	0.005	0.007	0.010	0.011	0.013	0.015
μ_{CD}	0.061	0.077	0.091	0.107	0.128	0.151
σ_{CD}	0.002	0.002	0.003	0.003	0.003	0.004
μ_{CM}	-0.021	-0.024	-0.025	-0.026	-0.028	-0.031
σ_{CM}	0.001	0.002	0.003	0.003	0.004	0.005

The standard deviations, σ, are presented as error bars in the C_L-α, C_D-α, and C_M-α plots provided in Fig. 6, but are difficult to observe for C_L and C_D due to their relatively small magnitude. Overall, the agreement between the experimental studies and the time-averaged CFD results are satisfactory. The slope of the predicted C_L-α curve is larger than that predicted by the experiments. Larger variations are predicted by the simulations than those observed in the experiments. The C_L predictions are in very good agreement with the experiments for α=10° and 11°, but exceed the measurements at the larger values of α. The C_D predictions are nearest the experimental results of the free transition setup even though the simulations assume the flowfield is fully turbulent. This is somewhat surprising considering that the C_p predictions generally agree with the 110 μm grit tape experimental findings.

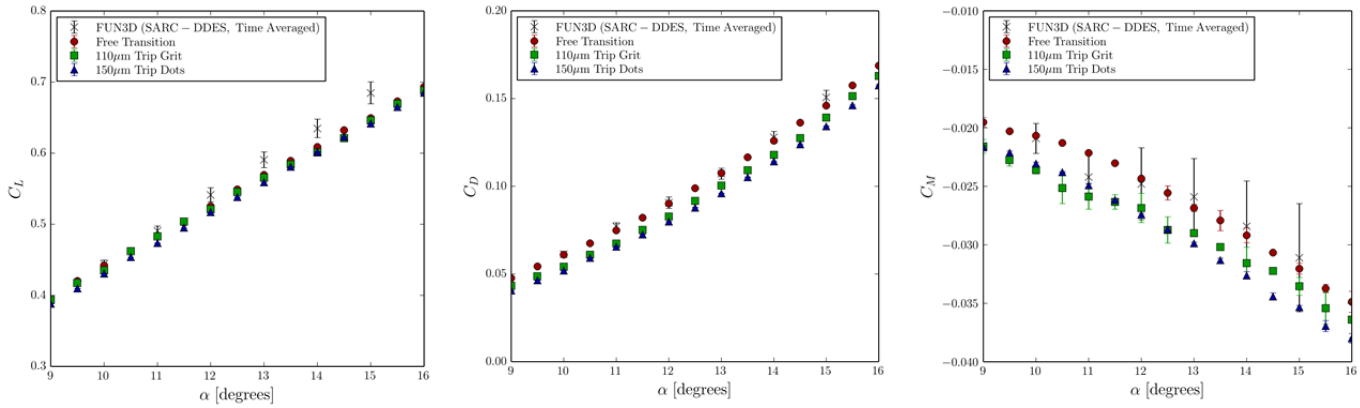

a) C_L-α **b) C_D-α** **c) C_M-α**

Figure 6: Time-averaged SARC-DDES predictions and experimental measurements of C_L, C_D, and C_M plotted versus α.

The time-averaged C_p distributions at root chord locations of x/c_r=0.100, 0.200, 0.295, 0.405, 0.500, and 0.600 are provided in Figs. 7-12 for the six values of α simulated. The unsteady (SARC-DDES) simulations are computed using the fine grid, but provide predictions less correlated with the experiements. Peak C_p predictions at streamwise locations with the primary vortex present are generally lower than that observed in the experiments for every α. The influence of the vortex on the C_p distributions is wider, but shallow and less intrusive to the outer flow region than the experimental results and the steady-state SARC predictions.

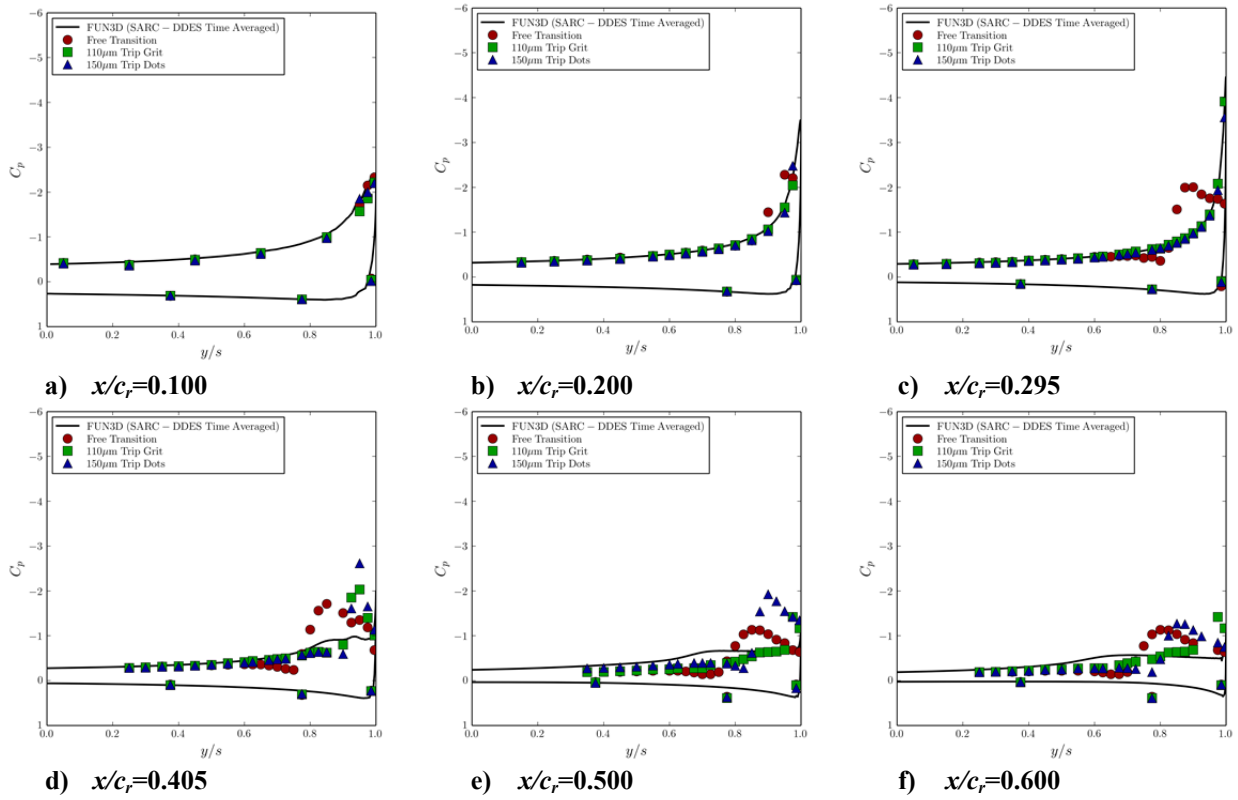

a) x/c_r=0.100 b) x/c_r=0.200 c) x/c_r=0.295

d) x/c_r=0.405 e) x/c_r=0.500 f) x/c_r=0.600

Figure 7: Time-averaged SARC-DDES C_p comparisons for α=10° at six x/c_r locations.

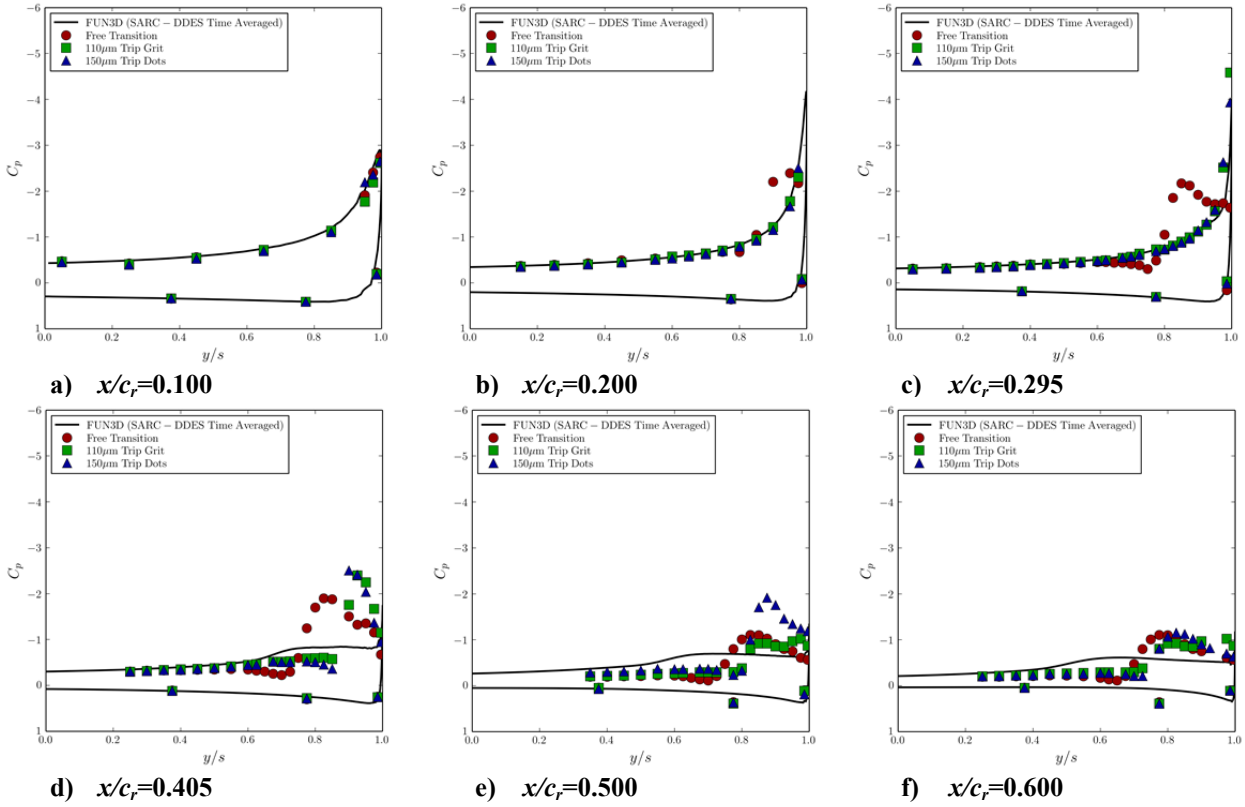

a) x/c_r=0.100 b) x/c_r=0.200 c) x/c_r=0.295

d) x/c_r=0.405 e) x/c_r=0.500 f) x/c_r=0.600

Figure 8: Time-averaged SARC-DDES C_p comparisons for α=11° at six x/c_r locations.

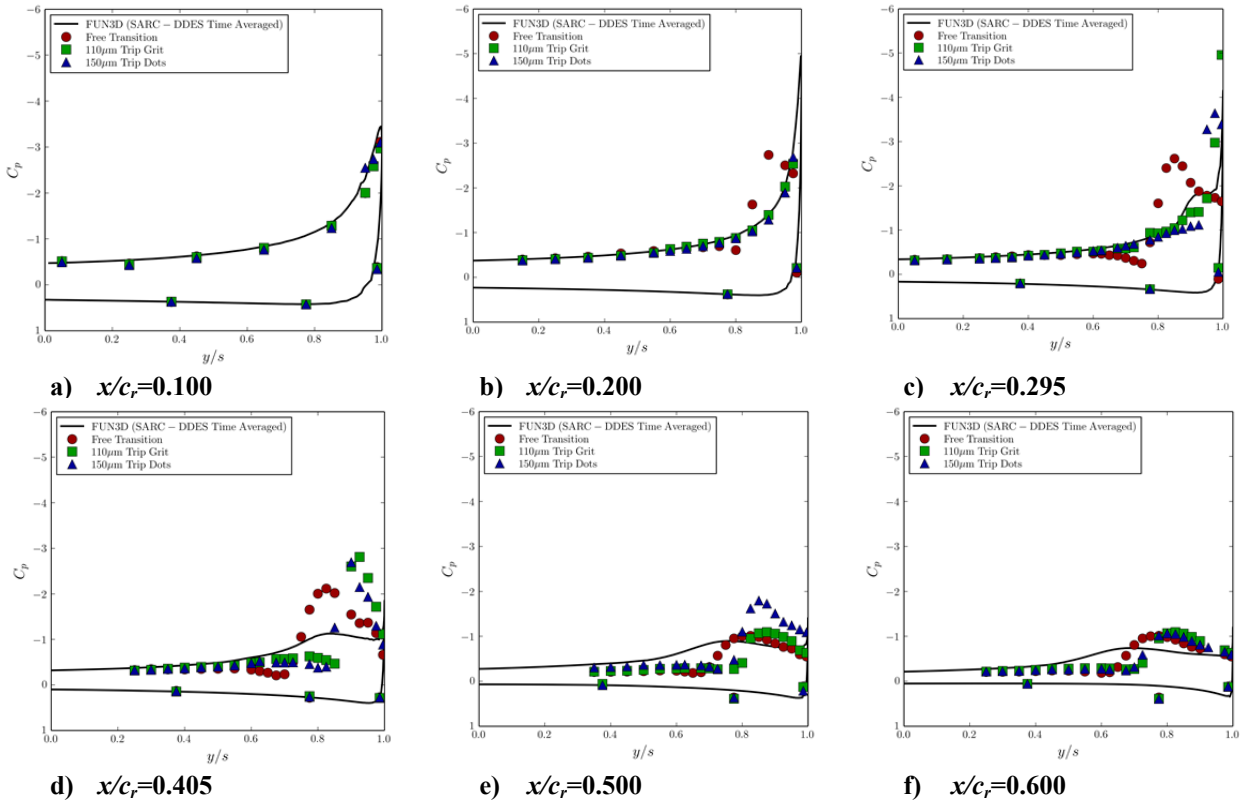

a) x/c_r=0.100 b) x/c_r=0.200 c) x/c_r=0.295

d) x/c_r=0.405 e) x/c_r=0.500 f) x/c_r=0.600

Figure 9: Time-averaged SARC-DDES C_p comparisons for α=12° at six x/c_r locations.

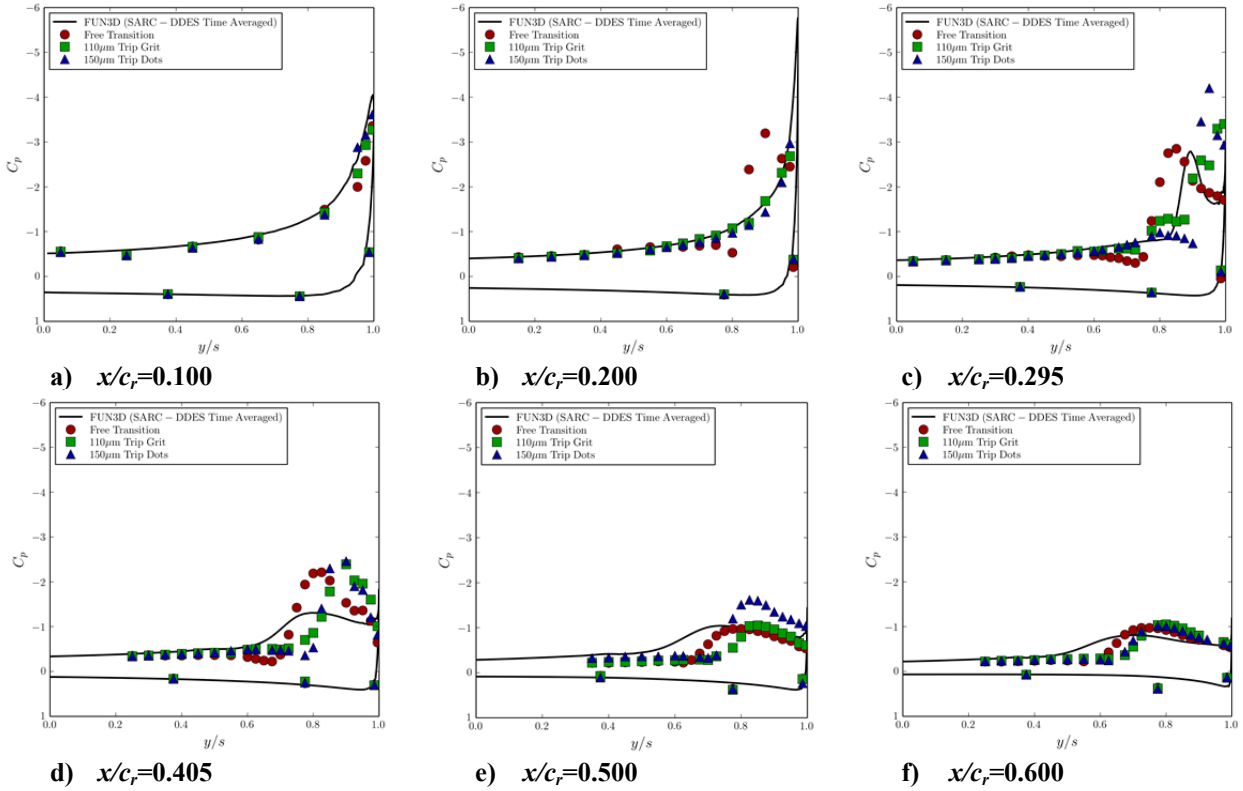

a) x/c_r=0.100 b) x/c_r=0.200 c) x/c_r=0.295

d) x/c_r=0.405 e) x/c_r=0.500 f) x/c_r=0.600

Figure 10: Time-averaged SARC-DDES C_p comparisons for α=13° at six x/c_r locations.

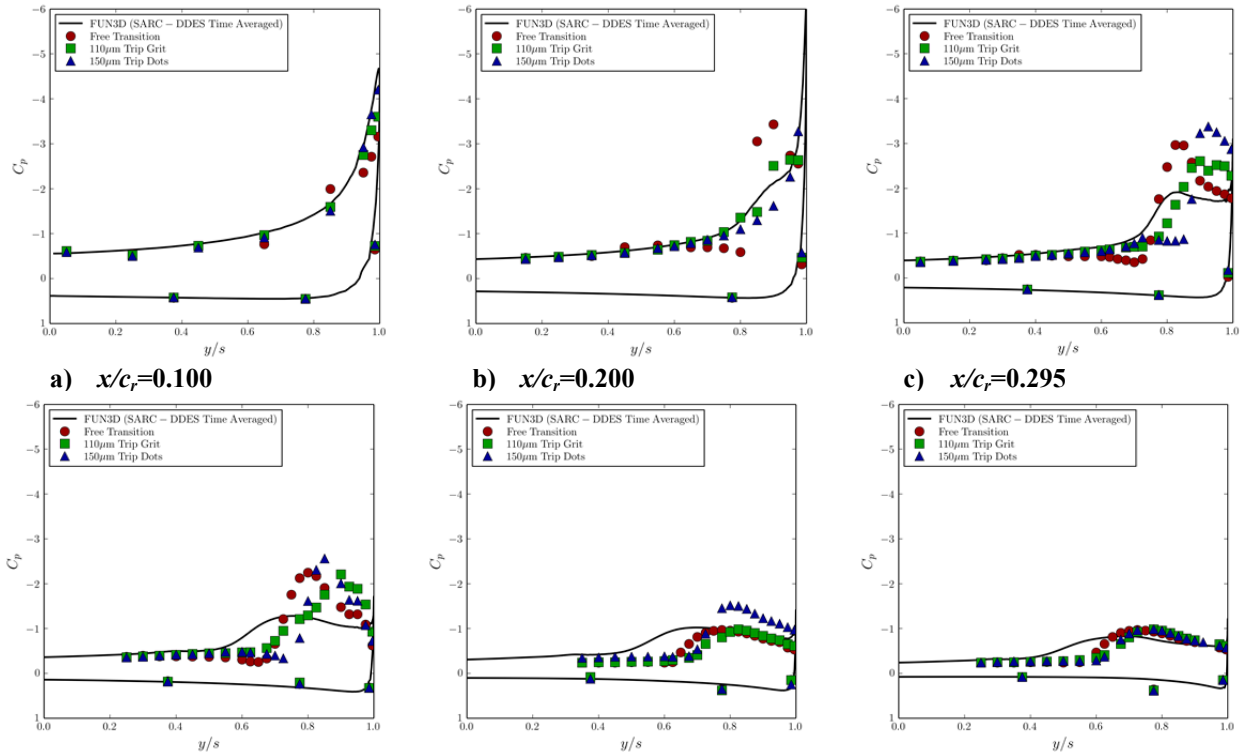

a) x/c_r=0.100 b) x/c_r=0.200 c) x/c_r=0.295

d) x/c_r=0.405 e) x/c_r=0.500 f) x/c_r=0.600

Figure 11: Time-averaged SARC-DDES C_p comparisons for α=14° at six x/c_r locations.

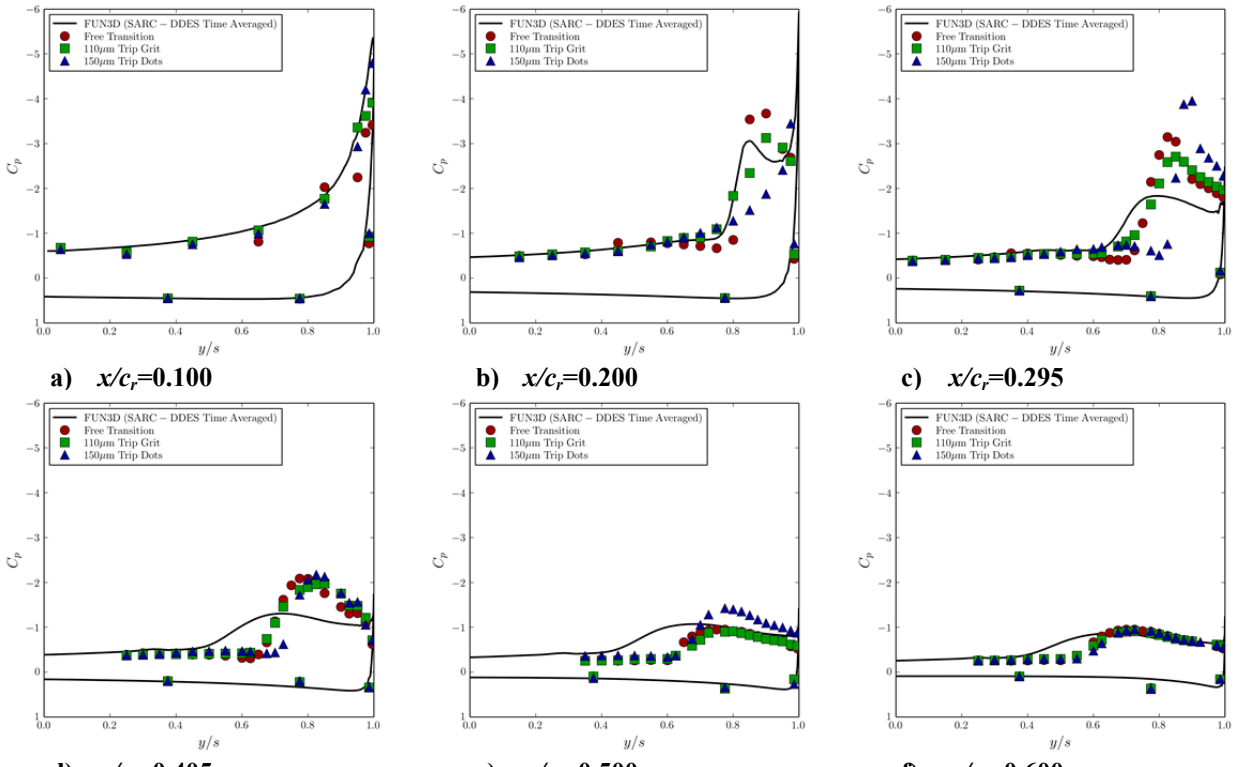

a) x/c_r=0.100 b) x/c_r=0.200 c) x/c_r=0.295

d) x/c_r=0.405 e) x/c_r=0.500 f) x/c_r=0.600

Figure 12: Time-averaged SARC-DDES C_p comparisons for α=15° at six x/c_r locations.

C. Unsteady Results

In theory, a hybrid model has a steady RANS zone, but the edge of this zone will be perturbed by the unsteady motion of the LES region effectively making the RANS region and URANS region[1]. Without this unsteady contamination of the RANS region, pressure measurements from SARC-DDES simulations would lack frequency content. In this section, we present the time histories and frequency content of unsteady responses of force and moment coefficients and C_p located at the Kulite sensor locations using power spectral density (PSD) plots of the SARC-DDES predictions.

Unsteady results are presented as time histories and PSDs where each is computed using the discrete fast Fourier transform (FFT) function in Python[19]. Raw FFT output was scaled via $PSD(I) = \frac{2\Delta t}{N}|FFT(I)|^2$ with units of $[I]^2\times[Hz]^{-1}$ where [I] is the unit of measure for the signal, Δt is the time step, and N is the number of points. PSDs of the experimental measurement time histories, provided by Hövelmann et al.[18], are post-processed similarly for comparison to eliminate any inconsistencies between analysis approaches. The PSDs are filtered by averaging every 20 and 10 values in the PSD responses along with their corresponding frequencies in the experimental and computational results respectively.

The force (C_L, C_D) and moment (C_M) coefficient time histories and PSDs from SARC-DDES simulations are presented in Fig. 13. The magnitude of the unsteadiness increases with increasing α for all of the coefficients as seen in the time history plots of Fig. 13(a-c) and through an increase of the peak magnitudes in the PSDs of Fig. 13(d-f). The frequency corresponding to the maximum amplitude oscillations decreases with increasing α. The main source of unsteadiness in the force and moment coefficients is the shedding of the primary vortex on the upper surface of the wing. The size of the primary vortex on the upper surface of the wing is known to increase with increasing α at a constant Mach number and Reynolds number causing the turnover time of that vortex to increase resulting in a reduction of the unsteady frequency response in the global forces and moments.

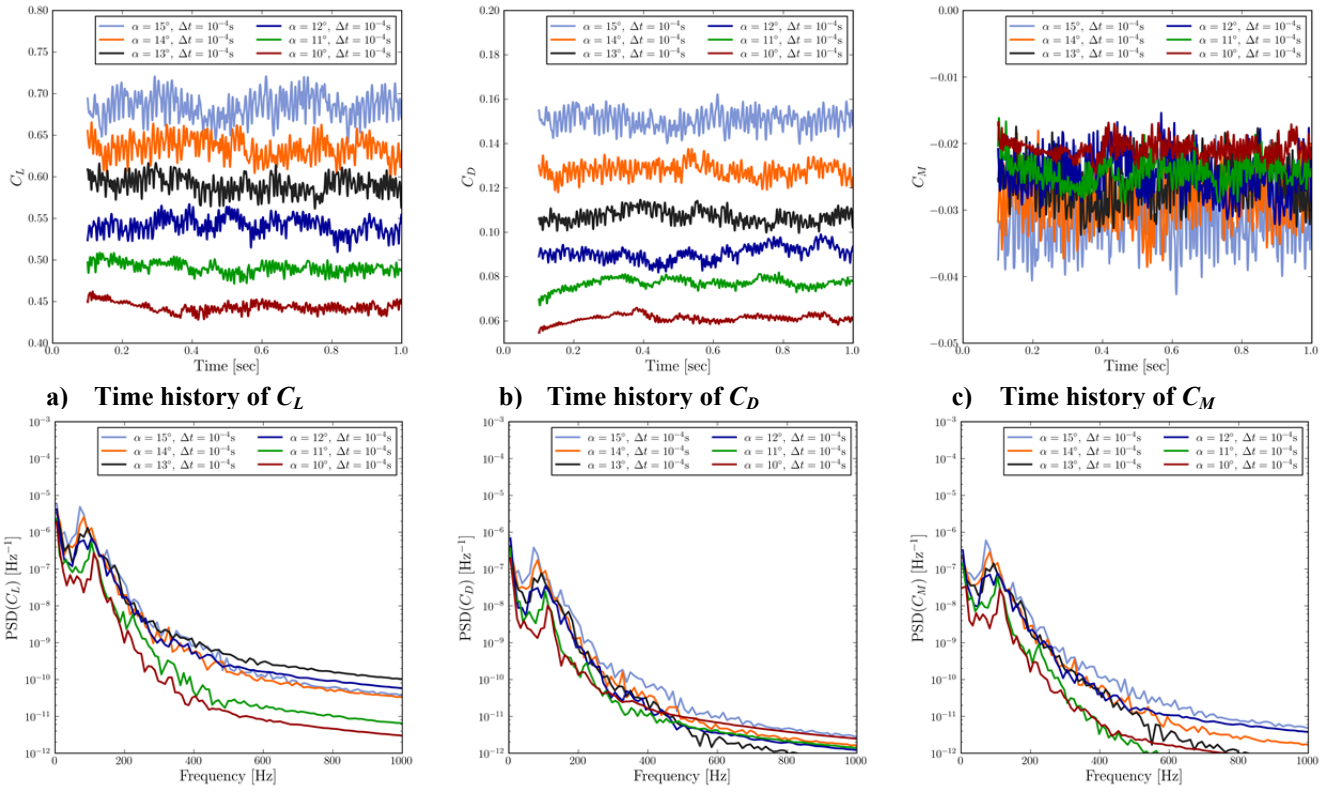

a) Time history of C_L **b) Time history of C_D** **c) Time history of C_M**

d) PSD of C_L **e) PSD of C_D** **f) PSD of C_M**

Figure 13: Simulated time histories (a-c) and PSDs (d-f) of force and moment coefficients C_L, C_D, and C_M.

The global unsteadiness due to this large-scale vortical motion of the primary vortex is predicted in the 100 Hz range for the values of α simulated. A scaling for the force and moment peak frequencies is observed to generate a relatively constant modified Strouhal number of:

$$St_\alpha = \frac{f^{peak}\bar{c}}{U_\infty}\sin\alpha \approx 0.3. \quad (3)$$

The results for the modified Strouhal number at the six values of α are presented in Table 5. It is clear that the effective wake width of $\bar{c}\sin\alpha$ is a more appropriate lengthscale for this study.

Table 5: Predicted variation of standard, *St*, and modified Strouhal number, St_α, with angle of attack, α.

α [deg.]	10°	11°	12°	13°	14°	15°
f^{peak} [Hz]	112	105	105	93.9	82.8	71.7
$St = \frac{f^{\text{peak}}\bar{c}}{U_\infty}$	1.75	1.65	1.64	1.47	1.30	1.13
$St_\alpha = \frac{f^{\text{peak}}\bar{c}}{U_\infty}\sin\alpha$	0.305	0.314	0.343	0.332	0.314	0.291

Time history measurements for pressure were provided by TUM, from the 110 µm trip grit experiments, for eight Kulite locations on the upper surface of the wing for α=12°, 13°, 14°, 15°, and are used to for PSD comparisons to CFD predictions. The time histories for C_p at the Kulite locations are presented in Fig. 14 for the inboard locations and Fig. 15 for the outboard locations with an image of the wing indicating where these sensors are located on the upper surface using matching colors to their corresponding time history responses. The predicted responses that lack periodic content are omitted in the PSD comparisons.

Focusing on Fig. 14, for the inboard responses, the simulated C_p response at the Kulite 1 location demonstrates unsteadiness for α=15°, but shows very little frequency content for the other values of α. The predicted response at the Kulite 2 location demonstrates unsteadiness at all α conditions, but does not demonstrate obvious frequency content for α=12°. The simulated responses at the Kulite 3 and 4 locations appear to be more representative of the frequency content measured experimentally.

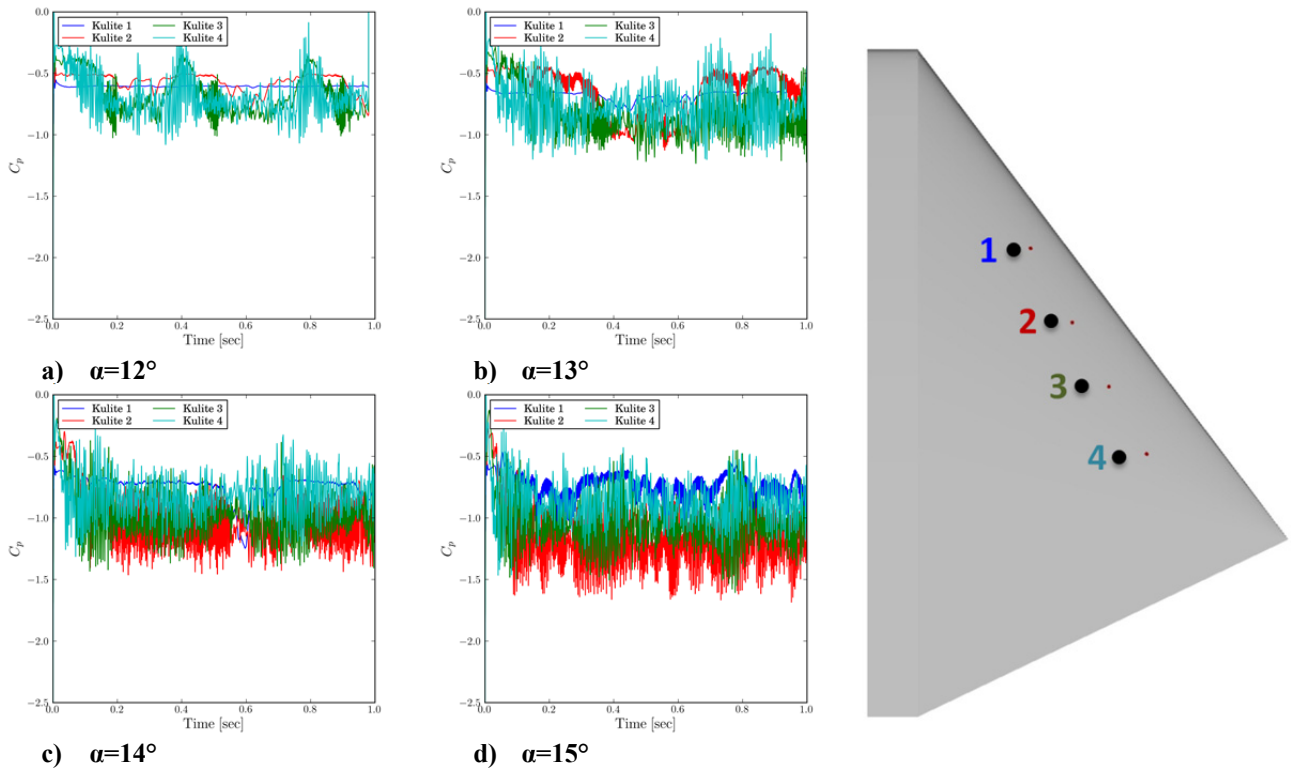

Figure 14: Simulated time histories of surface C_p sampled at the inboard Kulite locations.

For the outboard responses presented in Fig. 15, the simulated responses at the Kulite 5 location do not exhibit unsteadiness at the α=12° and 13° conditions. The simulated response at the Kulite 6 location demonstrates an intermittent response for α=12° and 13°. The simulated responses for the locations of Kulite 7 and 8 demonstrate frequency content for all α, but also reveal an intermittent or bi-modal response for α=12° and 13°. All of these probe locations are in the viscous sub-layer of a fully turbulent boundary layer that is governed by the SARC turbulence model. However, the pressure at the edge of the boundary layer is projected on to the wing surface. We believe that the very low frequency intermittent behavior may be caused by the turbulence model switching between RANS and LES modes at the edge of the boundary layer in the vicinity of the Kulite 5 and 6 locations.

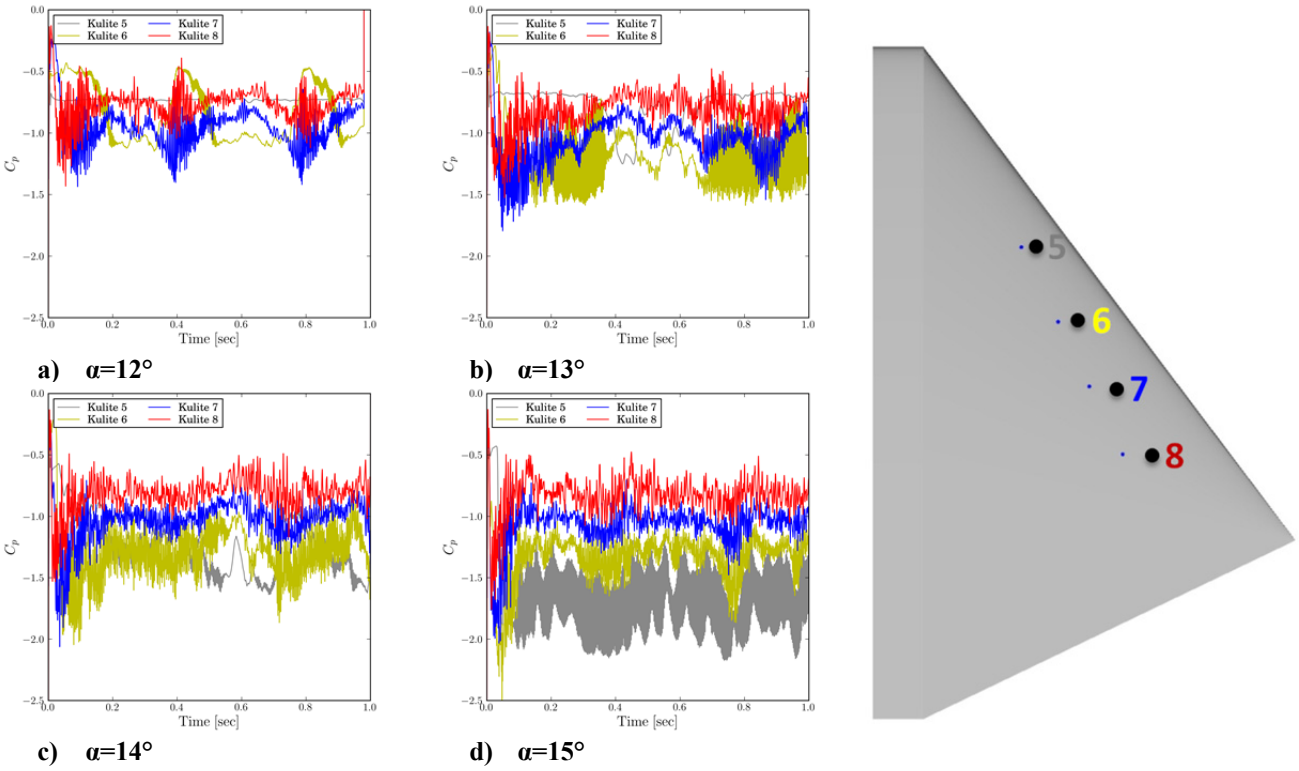

Figure 15: Simulated time histories of surface C_p sampled at the outboard Kulite locations.

All of the C_p signals that exhibited unsteadiness appear to have a wide frequency spectrum of content based on the PSD plots given in Figs. 16-23 along with the experimental measurements provided by TUM with the 110 μm grit tape at α=12°, 13°, 14°, and 15°. In general, most of the PSDs of the TUM wind tunnel data show a steady decline in frequency content with few discernable peaks. The peaks in the experimental PSDs are most prevalent at the x/c_r=0.600 location, however. The comparisons of TUM data to the SARC-DDES predicted PSDs of the forward Kulite positions 1, 2, 5, and 6 have been omitted for brevity and because the lack of frequency content in the SARC-DDES simulations at the forward Kulite locations generates erratic FFT output not suitable for comparison.

Figure 16 compares the PSDs for the C_p measured at Kulite positions 3 (x/c_r=0.5, y/s=0.65) and 4 (x/c_r=0.600, y/s=0.65) and Figure 17 compares those measured at Kulite positions 7 (x/c_r=0.500, y/s=0.75) and 8 (x/c_r=0.600, y/s=0.75) for α=12°. The predicted PSD responses for Kulite positions 3 and 4 show discernable peaks at approximately 300 Hz and 200 Hz respectively whereas the experimental results show no peak at Kulite 3 and a small change in slope at approximately 250 Hz for Kulite 4. At the further outboard Kulite locations, the CFD prediction did not match the experiment well for Kulite 7, but was in very good agreement for the Kulite 8 location both with peak frequency observed at approximately 200 Hz, and for the slope of the PSD at higher frequencies.

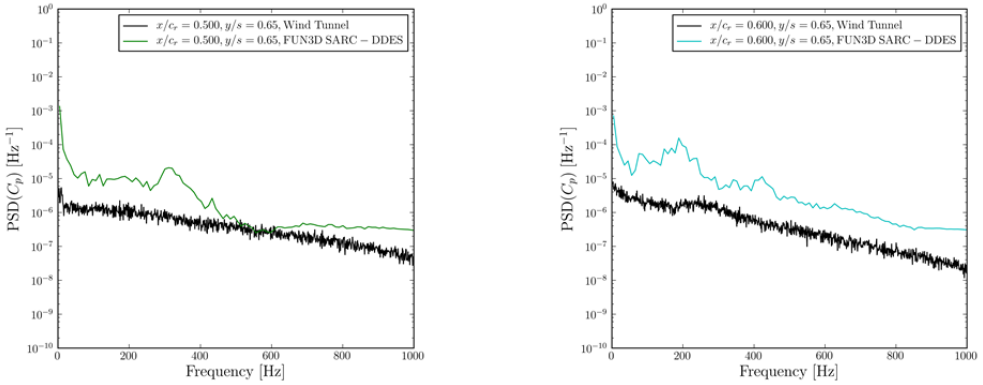

a) Kulite 3 (x/c_r=0.500, y/s=0.65) **b) Kulite 4 (x/c_r=0.600, y/s=0.65)**

Figure 16: Surface C_p PSDs sampled at the inboard Kulite locations for the α=12° case.

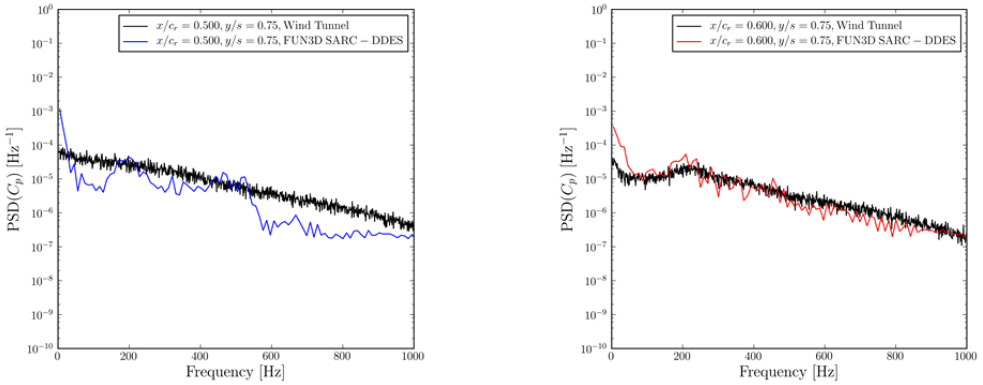

a) Kulite 7 (x/c_r=0.500, y/s=0.75) **b) Kulite 8 (x/c_r=0.600, y/s=0.75)**

Figure 17: Surface C_p PSDs sampled at the outboard Kulite locations for the α=12° case.

Figure 18 compares the PSDs for the C_p measured at Kulite positions 3 and 4 and Figure 19 compares those measured at Kulite positions 7 and 8 for α=13°. The predicted PSD response for Kulite positions 3 shows some broadband response from 150-450 Hz while the predicted Kulite 4 response peaks at approximately 180 Hz. The experimental result shows no peak at Kulite 3 and a peak at approximately 225 Hz for Kulite 4. At the further outboard Kulite locations, the CFD predictions matched the slope for Kulite 7 and 8, but failed to predict the clear peak at 200 Hz seen in the experimental response.

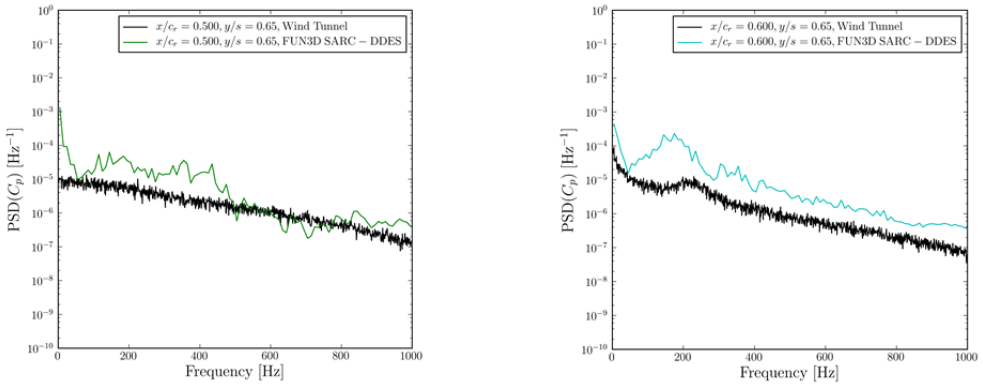

a) Kulite 3 (x/c_r=0.500, y/s=0.65) **b) Kulite 4 (x/c_r=0.600, y/s=0.65)**

Figure 18: Surface C_p PSDs sampled at the inboard Kulite locations for the α=13° case.

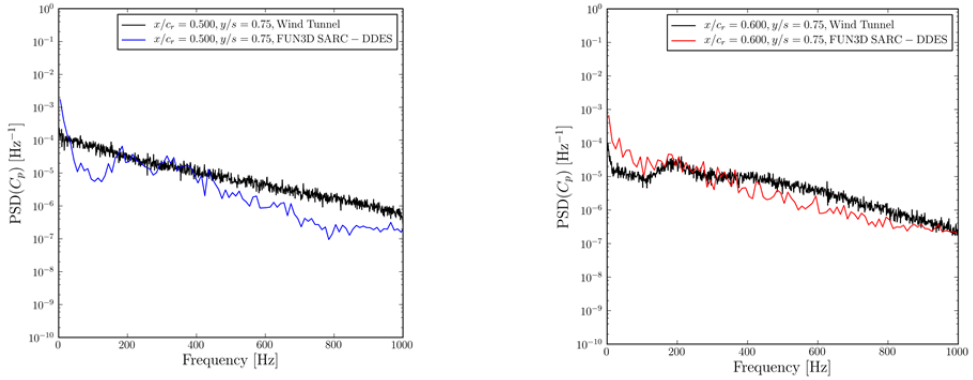

a) Kulite 7 (x/c_r=0.500, y/s=0.75) **b) Kulite 8 (x/c_r=0.600, y/s=0.75)**

Figure 19: Surface C_p PSDs sampled at the outboard Kulite locations for the α=13° case.

Figure 20 compares the PSDs for the C_p measured at Kulite positions 3 and 4 and Figure 21 compares those measured at Kulite positions 7 and 8 for α=14°. Again, the predicted PSD response for Kulite positions 3 shows some broadband response from 150-450 Hz while the predicted Kulite 4 response peaks at approximately 160 Hz. The experimental result shows no peak at Kulite 3 and a peak at approximately 180 Hz for Kulite 4. At the further outboard Kulite locations, the CFD predictions matched the slope for Kulite 7 and 8, but failed to predict the modest peak at approximately 200 Hz seen in the experimental response.

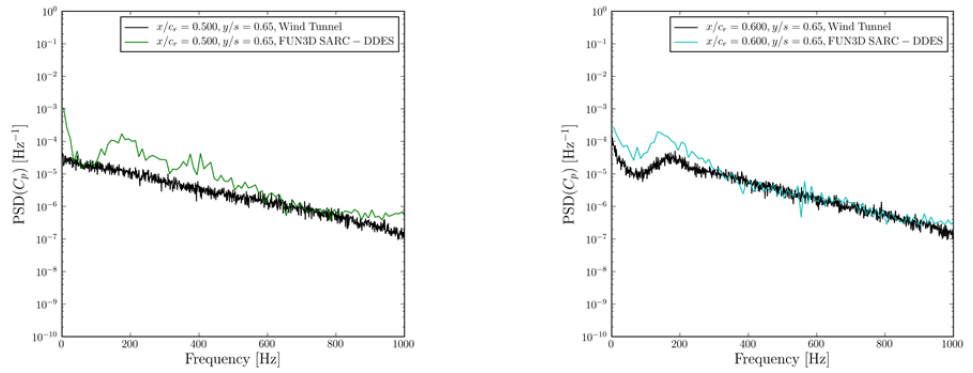

a) Kulite 3 (x/c_r=0.500, y/s=0.65) **b) Kulite 4 (x/c_r=0.600, y/s=0.65)**

Figure 20: Surface C_p PSDs sampled at the inboard Kulite locations for the α=14° case.

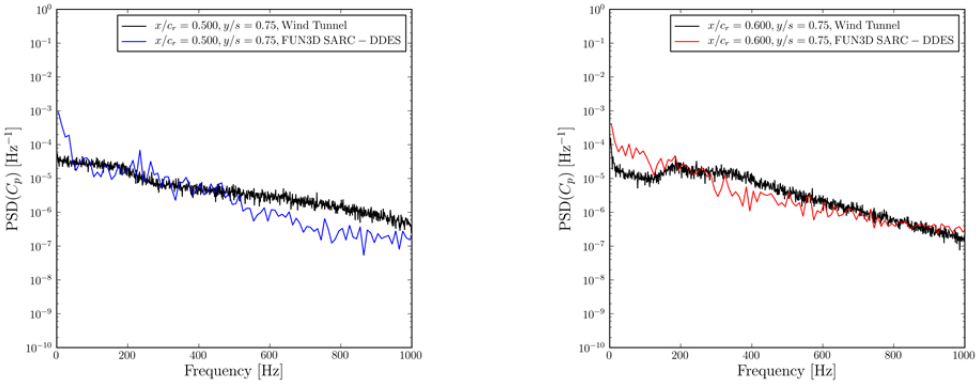

a) Kulite 7 (x/c_r=0.500, y/s=0.75) **b) Kulite 8 (x/c_r=0.600, y/s=0.75)**

Figure 21: Surface C_p PSDs sampled at the outboard Kulite locations for the α=14° case.

Figure 22 compares the PSDs for the C_p measured at Kulite positions 3 and 4 and Figure 23 compares those measured at Kulite positions 7 and 8 for α=15°. The predicted PSD response for Kulite position 3 agrees well for the steadily decaying experimental response. The predicted Kulite 4 response peaks at approximately 180 Hz, as does the experiment. However, the peak amplitude of the CFD response is a decade larger than the experimental result. At the further outboard Kulite locations, the CFD predictions matched the slope for Kulite 7 and 8, but failed to predict the change in slope at approximately 200 Hz seen in the experimental response.

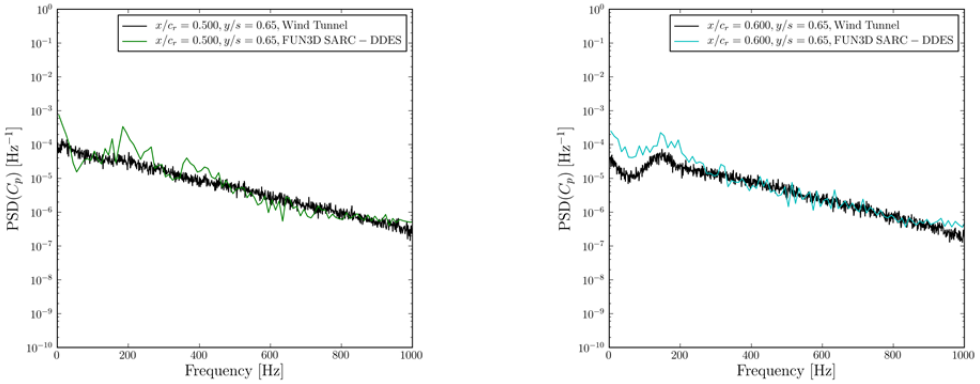

a) Kulite 3 (x/c_r=0.500, y/s=0.65) **b) Kulite 4 (x/c_r=0.600, y/s=0.65)**

Figure 22: Surface C_p PSDs sampled at the inboard Kulite locations for the α=15° case.

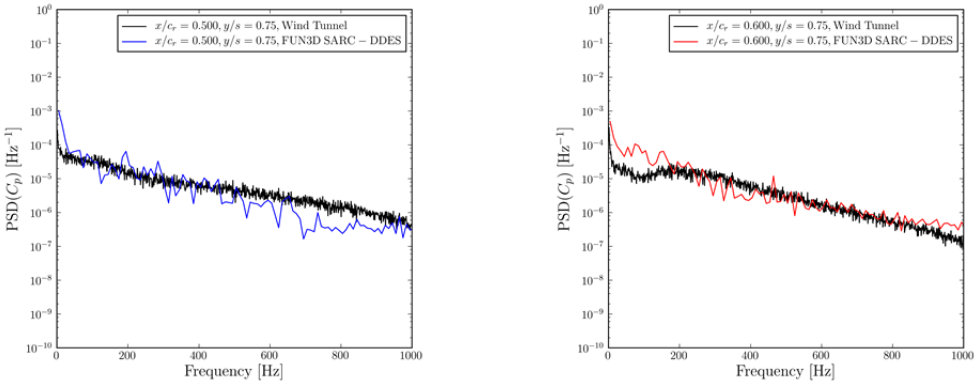

a) Kulite 7 (x/c_r=0.500, y/s=0.75) **b) Kulite 8 (x/c_r=0.600, y/s=0.75)**

Figure 23: Surface C_p PSDs sampled at the outboard Kulite locations for the α=15° case.

The simulation at α=12° was run for an additional 5.5 s of physical time (totaling 6.5 s) to assess the duration of the time history on the frequency-domain analysis. The longer time history allows for more frequency resolution in the frequency-domain analysis and allows for more periods of low-frequency content to be simulated. The C_p time histories for the simulated Kulite positions of 3, 4, 7, and 8 were analyzed in an identical manner as before and the PSD plots are presented in Fig. 24 for the inboard locations and Fig. 25 for the outboard locations. The almost ideal agreement that we observed for Kulite 8 for the short time history still holds for frequencies below 200 Hz, but the slope of the PSD after the primary peak is no longer in agreement with the experimental findings.

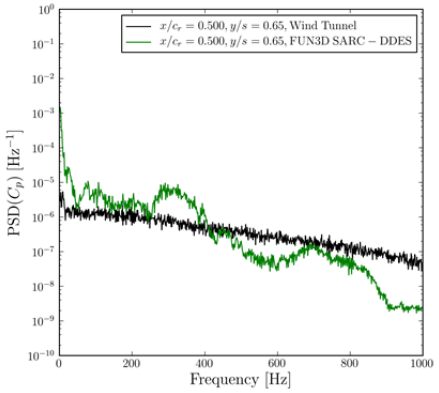

a) Kulite 3 (x/c_r=0.500, y/s=0.65)

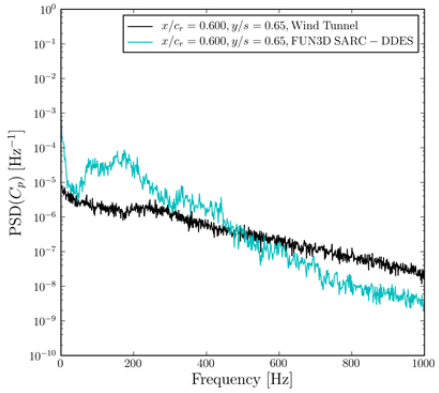

b) Kulite 4 (x/c_r=0.600, y/s=0.65)

Figure 24: Surface C_p PSDs sampled at the inboard Kulite locations for the α=12° case run for 6.5 s.

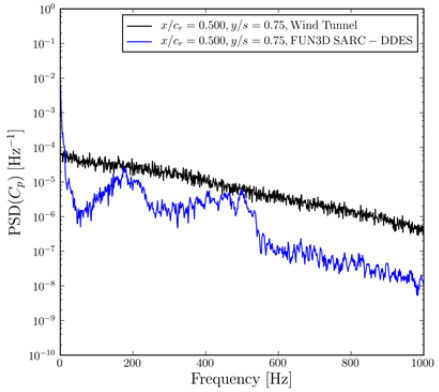

a) Kulite 7 (x/c_r=0.500, y/s=0.75)

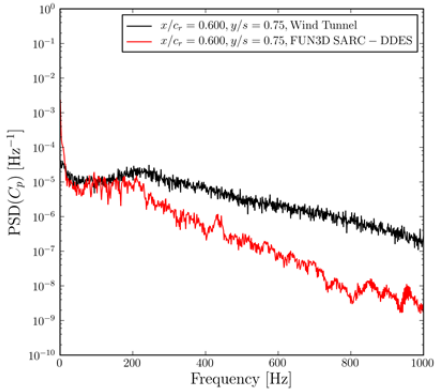

b) Kulite 8 (x/c_r=0.600, y/s=0.75)

Figure 25: Surface C_p PSDs sampled at the outboard Kulite locations for the α=12° case run for 6.5 s.

D. Separation Prediction

The separation onset from the CFD results were obtained using the methodology of Simpson[2] by plotting the probability of flow reversal at different chord- and span-wise locations for the α values simulated. The skin friction vector is recorded at these locations at a frequency of 1 kHz (every 10 time steps) and probabilities were then calculated based on the sign of $C_{f,y}$ at discrete grid locations. Figure 26 provides the probability distributions, $\bar{\gamma}$, for the ten chord-wise locations for each α along with the thresholds for intermittent transitory detachment (ITD) and transitory detachment (TD). These distributions present what portion of each chord-wise distribution is separated and allow for quick recognition of the primary and co-rotating inboard vortices that originate from the leading edge. For a fixed α, the inboard vortex moves further inboard on the y/s coordinate with increasing chord-wise location x/c_r. Also as α is increased, the primary vortex separation location moves upstream, e.g., the location of primary vortex separation at α=10° is in the proximity of x/c_r=0.305, it is between x/c_r=0.250-0.295 for α=11°-13°, and upstream of x/c_r=0.250 for α=14° and 15°. As the α is increased, the inboard vortex moves further inboard, becomes wider, and presents higher probabilities of flow reversal. In Fig. 26(a), evidence exists of an inboard vortex bifurcating from the primary vortex at the x/c_r=0.450 location for α=10°. This inboard vortex is clearly bifurcated from the primary vortex in Fig. 26(b) at α=11°. As α is increased further, the formation of the inboard vortex moves upstream where it is present as far forward as x/c_r=0.250 at α=15°. The response of $\bar{\gamma}$ for α=13° is somewhat peculiar as it does not follow the trend progressing from the other α values simulated and reveals an inboard vortex that persists for a significant portion of the sampled time exceeding the ITD threshold in some at some chord locations.

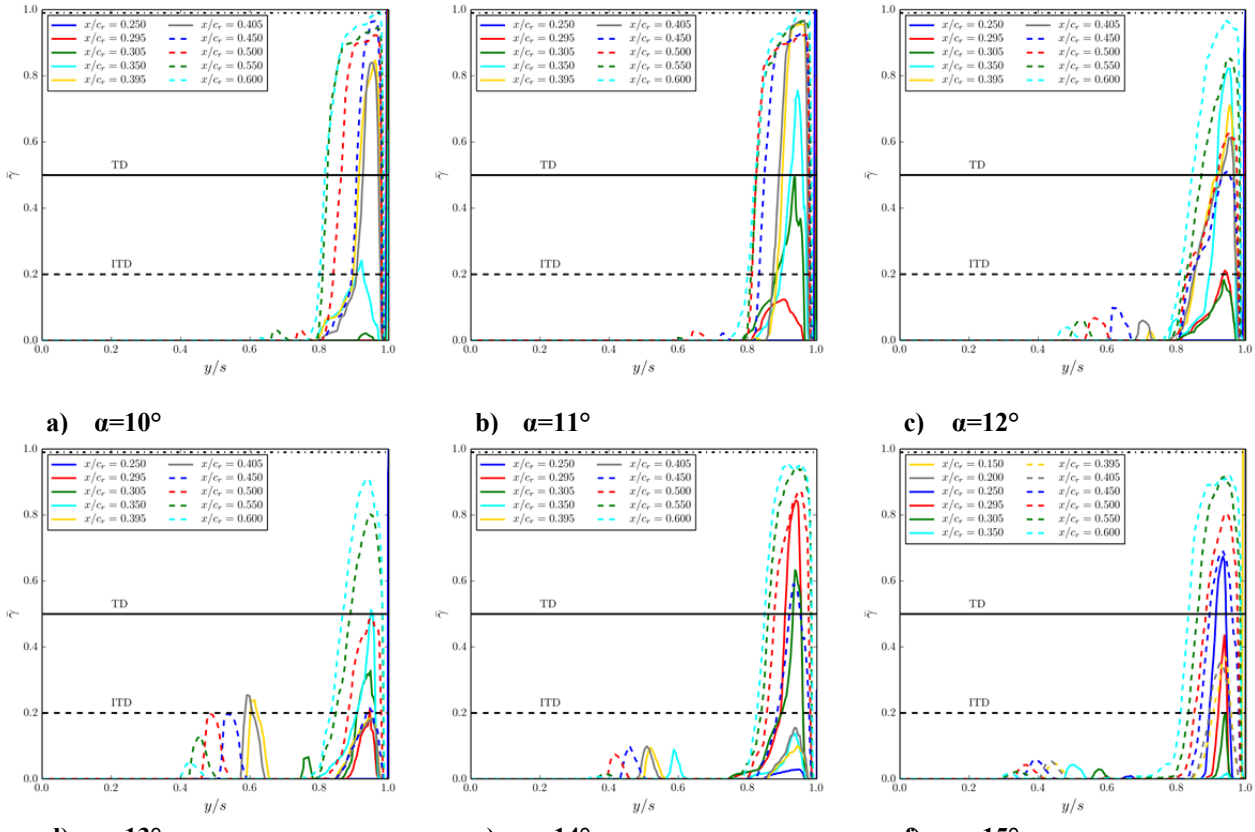

Figure 26: Distributions of the probability of flow reversal, $\overline{\gamma}$, from SARC-DDES predictions.

IV. Conclusion

As expected, our findings suggest that global quantities of C_L, C_D, and C_M are much easier to predict than locally measured quantities. During the grid refinement study, inconsistencies in the global force and moment coefficients as well as C_p distributions were observed when comparing the medium and fine grids. It is our opinion that the computational grids are a primary influence on these observations and that a lack of prismatic elements further away from the wing/peniche surface and a lack of resolution and isotropy in the focus region, just outside of the viscous boundary layer, are both areas of possible solution contamination. Lastly, the grid resolution in the wall-normal direction may have been too coarse to properly demonstrate adequate grid independence since y^+ was approximately unity for all three levels of grid instead of being systematically refined along with the surface discretization.

The steady-SARC results for C_p are in better agreement with the time-averaged wind tunnel measurements than the time-averaged SARC-DDES predictions with the finest grid, but neither is as correlated as the medium grid steady-SARC simulation results. The lack of a well-defined suction peak in the time-averaged C_p predictions may be due to the premature transition of prism to tetrahedral elements near the edge of the viscous boundary layer.

Acknowledgments

The experimental measurement data was provided in the framework of NATO STO Task Group AVT-183 by the Institute of Aerodynamics and Fluid Mechanics of Technische Universität München, München, Germany. The authors would like to thank all the members of the AVT-183 task group for providing direction and constructive criticisms and critiques of this work. The authors would like to thank the US DoD High Performance Computing Modernization Program and the ERDC DoD Supercomputing Resource Center for the use of Garnet. Lastly, we would like to thank the leadership and support of the US Air Force Test Center located at the 412th Test Wing at Edwards AFB, CA and the Arnold Engineering Development Complex located at Arnold AFB, TN.

References

[1]Tucker, P. G., Unsteady Computational Fluid Dynamics in Aeronautics, Springer, 2014.

[2]Simpson, R. L., "A review of some phenomena in turbulent flow separation," *Journal of Fluids Engineering*, Vol. 102, 1981, pp. 520-533.

[3]Boelens, O. J., Luckring, J. M., Knoth, F., Hovelmann, A., Breitsamter, C., Malloy, D. J., Deck, S., "Numerical and Theoretical Considerations for the Design of the AVT-183 Diamond-Wing Experimental Investigations," AIAA Paper 2015-XXXX, 53rd AIAA Aerospace Science Meeting, 2015.

[4]Anderson, W. K. and Bonhaus, D. L., "An Implicit Upwind Algorithm for Computing Turbulent Flow on Unstructured Grids," *Computers & Fluids*, Vol. 23, No. 1, 1994, pp. 1-21.

[5]Biedron, R. T., Derlaga, J. M., Gnoffo, P. A., Hammond, D. P., Jones, W. T., Kleb, B., Lee-Rausch, E. M., Nielsen, E. J., Park, M. A., Rumsey, C. L., Thomas, J. L., and Wood, W. A., *FUN3D Manual: 12.4-70371*, NASA/TM-2014-218179, http://fun3d.larc.nasa.gov, accessed April 2014.

[6]Spalart, P. R., Allmaras, S.R., "A One-Equation Turbulence Model for Aerodynamic Flows," AIAA paper 92-0439, 30th Aerospace Sciences Meeting & Exhibit, 1992.

[7]Shur, M. L., Strelets, M. K., Travin, A. K., and Spalart, P. R., "Turbulence Modeling in Rotating and Curved Channels: Assessing the Spalart−Shur Correction," *AIAA Journal*, Vol. 38, No. 5, 2000, pp. 784-792.

[8]Rumsey, C., *Turbulence Modeling Resource Website*, NASA Langley Research Center, accessed on September 2014, http://turbmodels.larc.nasa.gov.

[9]Dacles-Mariani, J., Zilliac, G. G., Chow, J. S., Bradshaw, P., "Numerical/Experimental Study of a Wingtip Vortex in the Near Field," AIAA Journal, Vol. 33, No. 9, 1995, pp. 1561-1568.

[10]Spalart, P. R., Deck, S., Shur, M. L., Squires, K. D., Strelets, M. Kh., Travin, A., "A new version of detached-eddy simulation, resistant to ambiguous grid densities," *Theoretical and Computational Fluid Dynamics*, Vol. 20, No. 3, 2006, pp. 181-195.

[11]Spalart, P. R., Jou, W.-H., Strelets, M., Allmaras, S. R., "Comments on the feasibility of LES for wings, and on a hybrid RANS/LES approach," Proceedings of first AFOSR international conference on DNS/LES, 1997.

[12]Simpson, R. L., "Turbulent Boundary-Layer Separation," *Annual Reviews of Fluid Mechanics*, Vol. 21, 1989, pp. 205-234.

[13]Jammalamadaka, A., Li, Z., Jaberi, F., "Numerical investigations of shock wave interactions with a supersonic turbulent boundary layer," *Physics of Fluids*, Vol. 26, No. 056101, 2014, pp. 1-30.

[14]Nichols, R. H, "Turbulence Models and Their Application to Complex Flows," University of Alabama Birmingham, Revision 4.01, 2010.

[15]Oberkampf, W. L. and Roy, C. J. Verification and Validation in Scientific Computing, Cambridge, 2010.

[16]Roach, P. J., "Perspective: a method for uniform reporting of grid refinement studies," *Journal of Fluids Engineering*, Vol. 116, 1994, pp.405-413.

[17]Hövelmann, A., Knoth, F. and Breitsamter, C., "Leading-Edge Roughness Effects on the Flow Separation Onset of the AVT-183 Diamond Wing Configuration", AIAA Paper 2015-XXXX, 53rd AIAA Aerospace Science Meeting, 2015.

[18]Hövelmann, A., Grawunder, M, Buzica, A. and Breitsamter, C., "Experimental Analyses on the Flow Field Characteristics of the AVT-183 Diamond Wing Configuration," AIAA Paper 2015-XXXX, 53rd AIAA Aerospace Science Meeting, 2015.

[19]Jones E., Oliphant E., Peterson P., *et al., SciPy: Open Source Scientific Tools for Python*, 2001-present, http://www.scipy.org/